ACS OMEGA

http://pubs.acs.org/journal/acsodf

Article

Theoretical Study on Carbon Monoxide Adsorption on Unsupported and γ-Al_2O_3-Supported Silver Nanoparticles: Size, Shape, and Support Effects

Kyoichi Sawabe* and Atsushi Satsuma

Cite This: *ACS Omega* 2022, 7, 4405−4412

Read Online

ACCESS | Metrics & More | Article Recommendations | Supporting Information

ABSTRACT: Nanoparticles (NPs) supported on metal oxides exhibit high catalytic activities for various reactions. The shape and oxidation state of such NPs, which are related to the catalytic activity, are often determined by the support. Herein, we conducted a density functional theory study on isolated silver (Ag) NPs and two types of Ag-NPs supported on gamma-aluminum oxide (γ-Al_2O_3). First, carbon monoxide (CO) adsorption on the isolated Ag NPs was investigated for decahedra (D_{5h}), icosahedra (I_h), and cuboctahedra (O_h) of various sizes. I_h and O_h NPs showed moderate size dependence, whereas D_{5h} NPs showed high size dependence when the height was below 1.4 nm. The enhancement of CO adsorption on D_{5h} NPs was attributed to the presence of superatomic states. Next, we performed geometrical optimization of Ag_{54}/γ-$Al_2O_3(110)$ with a decahedral shape. Two types of structures were obtained: amorphous Ag_{54}(A) and locally fivefold symmetrical Ag_{54}(B) structures. Both NPs on γ-$Al_2O_3(110)$ were found to be positively charged, but electron transfer to the support occurred only from the Ag atoms at the two bottom layers, and the upper part of NPs was relatively neutral. The enhancement of CO adsorption on Ag_{54}(B) disappeared due to loss of the high symmetry. In turn, the moderate size dependence of neutral isolated NPs can be applied.

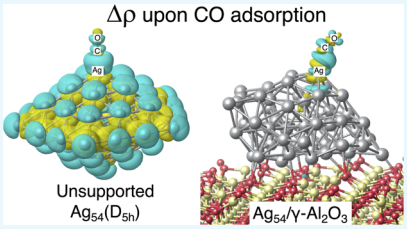

INTRODUCTION

Metal nanoparticles (NPs) supported on metal oxides exhibit high catalytic activity for various reactions owing to their sizes, shapes, oxidation states, and compositions.[1] A decrease in the size of metal NPs is accompanied by a change in the distribution of surface sites, such as the plane edge and corner.[2] If the electronic structure is not perturbed by a decrease in the NP size, the catalytic activity by the size effect can be discussed in the site distribution. When the size of NPs is in the range of several nanometers, the electronic state of the NPs becomes discrete. Therefore, the electronic state of each site of NPs differs from that of the bulk material.[3,4] This finite size effect depends on the type of metal, site, and adsorbed species. Carbon monoxide (CO) adsorption on the (111) surface of platinum (Pt) NPs is enhanced when the size is less than 1.6 nm, and such enhancement is observed on the (211) surface when the size is less than 1.2 nm.[4] The shape of NPs also affects the electronic states of the reaction sites because the discrete electronic states are affected by the potential determined by their shape. In particular, when the symmetry of NPs with a highly symmetric structure is lowered, the degenerate energy levels split.[5,6] This removal of degeneracy may change the catalytic activity.

A well-known example of size and support effects is the catalytic activity of gold (Au).[7−9] CO oxidation over Au NPs depends on not only the size but also the support. Au NPs for CO oxidation prefer reducible oxides, such as titanium dioxide (TiO_2) and iron (III) oxide (Fe_2O_3), as their support rather than irreducible oxides, such as aluminum oxide (Al_2O_3) and silicon dioxide (SiO_2).[10] Therefore, the oxidation states of Au NPs may be related to the activity, but it is yet to be clarified.[7] The support affects the shape of metal NPs. The activity of CH_4 combustion over Pd/Al_2O_3 depends on the phase of Al_2O_3. At an NP size of around 5 nm, Pd/α-Al_2O_3 and Pd/θ-Al_2O_3 show higher activity than Pd/γ-Al_2O_3 by a factor of 10.[11] Cs-S/TEM observations have shown a spherical structure for Pd/θ-Al_2O_3 and an amorphous-like structure for Pd/γ-Al_2O_3. The morphological change of NPs by the support is key to enhancing the activity. Thus, the influence of supports on metal NPs should be considered because the supports may induce charge transfer or deformation of the NP structure.

Ag/Al_2O_3[12] and Ag/SiO_2[13] show CO oxidation at low temperatures. According to a recent report, Ag NPs rather than a single-atom Ag have advantages over CO oxidation.[14] Ag NPs also show the size effect for CO oxidation.[12] In contrast to Au NPs, the CO oxidation activity of Ag NPs shows no strong support effect, indicating that CO oxidation proceeds on the active sites on Ag NPs.[12] Tamaru[15] reported that the oxygen and CO reaction occurs in a very limited area on Ag surfaces.

Received: November 4, 2021
Accepted: January 18, 2022
Published: January 28, 2022

In addition, the reaction rate for CO is of first order, whereas it is of zero order for the oxygen pressure. Therefore, CO adsorption can be used to probe the activity of CO oxidation.

In this study, we investigated whether Ag NPs have a morphological effect similar to that of Au NPs. First, CO adsorption was examined for various sizes of cuboctahedra, decahedra, and icosahedra. Among these models, the Ag_{54} decahedron showed superatom behavior to CO adsorption owing to its high symmetry, enhancing the adsorption strength. Then, the Ag_{54} decahedron was placed on the γ-$Al_2O_3(110)$ surface, and geometry optimization was performed. Two types of adsorbed structures were obtained: amorphous and locally fivefold symmetrical structures. Because the latter is deformed from a highly symmetrical structure, the superatomic behavior of the decahedron is lost. As a result, the enhancement of CO adsorption disappears. In turn, the moderate size dependence of neutral isolated NPs can be applied.

RESULTS AND DISCUSSION

CO Adsorption on Unsupported Ag NPs. The adsorption energy of CO was calculated on isolated Ag NPs with the shape of decahedron (D_{5h} symmetry), icosahedron (I_h symmetry), and cuboctahedron (O_h symmetry). Table 1 lists all adsorption energies of this work. A pentagonal decahedron was used as the smallest $Ag_{54}(D_{5h})$ model. As the size of this particle was increased by putting more atoms to the shell around it, the number of atoms changed from even to odd. Thus, we used Marks decahedra for the other sizes to avoid changing the spin state. However, the ground states of $Ag_n(D_{5h})$ (n = 100, 176, and 282) are singlet, and that of $Ag_{54}(D_{5h})$ is a triplet. The energy difference between the singlet and triplet of $Ag_{54}(D_{5h})$ is 0.01 eV, and the CO adsorption energies of these states differ by 0.01 eV. Thus, the difference between the triplet and singlet electronic states of $Ag_{54}(D_{5h})$ has little effect on the adsorption energy. Figure 1 shows the optimized structures of CO adsorbed on Ag NPs. All the *XYZ* coordinates of the optimized structures are listed in the Supporting Information. CO adsorption sites were chosen as the apex sites to compare the size and morphological effect on similar adsorption sites. CO adsorption was almost straight on all Ag NPs but tilted on $Ag_{176}(D_{5h})$ and $Ag_{147}(I_h)$ NPs.

Table 1. CO Adsorption Energies in eV[a]

	E_{total}	E_{DFT}	E_{disp}
Ag(111)	−0.214	0.092	−0.306
	D_{5h}		
Ag_{54} (fixed geometry)	−0.566	−0.438	−0.128
Ag_{54} (singlet)	−0.585	−0.472	−0.113
Ag_{54} (triplet)	−0.573	−0.472	−0.101
Ag_{100}	−0.474	−0.296	−0.178
Ag_{176}	−0.358	−0.144	−0.214
Ag_{282}	−0.327	−0.123	−0.204
	I_h		
Ag_{55}	−0.354	−0.230	−0.124
Ag_{147}	−0.297	−0.172	−0.125
Ag_{309}	−0.242	−0.101	−0.141
	O_h		
Ag_{55}	−0.406	−0.298	−0.108
Ag_{147}	−0.391	−0.191	−0.200
Ag_{309}	−0.362	−0.163	−0.198
	Ag NP on γ-Al_2O_3		
$Ag_{54}(B)/\gamma$-Al_2O_3	−0.481	−0.365	−0.116

[a] E_{DFT} and E_{disp} represent the contributions of the DFT and dispersion energies, respectively, to the adsorption energy. $Ag_{54}(B)/\gamma$-Al_2O_3 represents the Ag_{54} nanoparticle with a local fivefold symmetry site on a γ-$Al_2O_3(110)$ surface (*vide infra*).

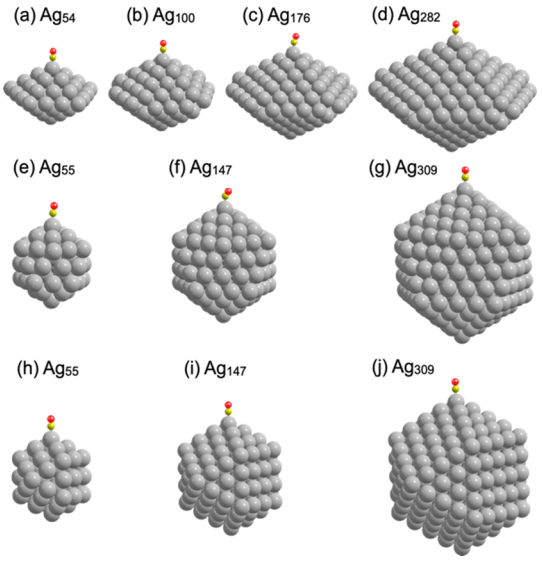

Figure 1. Optimized structures of Ag_n (n = 54−309) NPs with CO adsorbates with Ag NP symmetries of (a−d) D_{5h}, (e−g) I_h, and (h−j) O_h. Gray, dark yellow, and red balls represent Ag, C, and O, respectively.

Figure 2a,b shows the CO adsorption energy as a function of NP width and height, respectively. The width was defined as twice the length of the distance from the center to the farthest atom, and the height was taken from the topmost atom to the bottommost atom (see Figure S1). The dimensions of each NP are listed in Table S1. In general, the width (diameter) is often used as the size of NPs measured by TEM observation. However, it is inappropriate as a descriptor for CO adsorption on NPs with various shapes, such as the pentagonal decahedron, icosahedron, and octahedron. Decahedron is an oblate shape, and icosahedron and octahedron are spherical. Even if the equatorial diameters of the sphere and oblate are the same, and their polar diameters are different, the potential

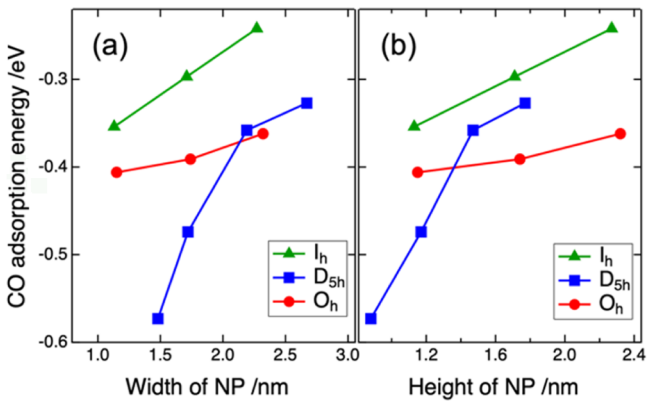

Figure 2. CO adsorption energy as a function of the (a) width and (b) height of NPs. Adsorption energies on decahedron (D_{5h}), cuboctahedron (O_h), and icosahedron (I_h) are indicated by blue, red, and green marks and lines, respectively.

https://doi.org/10.1021/acsomega.1c06208
ACS Omega 2022, 7, 4405−4412

change due to this difference predominantly affects the electronic states along the polar direction. For example, when metal NPs have a superatomic state, the deformation of the sphere to the oblate splits the degenerate state.[5] Thus, to analyze the catalytic activity at the apex site of NPs with various shapes, height is a better size descriptor (Figure 2b).

In general, the adsorption energy of CO for large-sized NPs is equal to that for the bulk material.[3,29,30] Thus, the trend of adsorption energy for larger NPs is similar to that of the bulk material. Because the coordination number (CN) of the top site of O_h NPs is five, and that of D_{5h} NPs is six, CO adsorption on O_h NP is stronger than that on D_{5h} NP with the same size of O_h NP. Nonetheless, no difference in adsorption energy was observed between O_h and D_{5h} NPs at a width of 2 nm. On the other hand, using the width as a size descriptor, CO adsorption on O_h NP was stronger than on D_{5h} NP, and the adsorption energy of D_{5h} was closer to that of I_h NP (CN = 5) than that of O_h NP. This trend applies to the adsorption on NPs with a height of more than 1.4 nm.

Both O_h and I_h NPs showed a moderate size dependence of CO adsorption, and the slope of the energy dependence on the height was larger for I_h than O_h. Both NPs converged to the same adsorption energy when the size was further decreased. In contrast, the slope of the size effect for D_{5h} NPs abruptly changes when the height is less than 1.4 nm. This increased size effect for CO adsorption is unique to the D_{5h} NP symmetry.

Boosted Size Effect of CO Adsorption. First, the strain effect of the D_{5h} NP was investigated because the enhancement of CO adsorption by multiple twinning in Au D_{5h} NPs is attributed to the strain effect at the adsorption site.[31] Fivefold-twinned decahedral Au NPs are intrinsically strained.[32] On the other hand, silver forms twinned particles easily owing to its low twin boundary energy.[33] To check the strain effect on the adsorption, the geometry optimization of CO adsorbed on the $Ag_{54}(D_{5h})$ NP was conducted by fixing only the NP structure to the isolated Ag_{54} NP. The resultant binding energy was 0.57 eV, which is the same as that obtained from the full geometry optimization. Thus, the fivefold twinned decahedral Ag does not show any strain effects on CO adsorption.

Next, we examined whether the boosted size effect originates from the electronic structure of the small D_{5h} NPs. Energy decomposition was performed for the adsorption energies of all CO adsorbed systems, including CO adsorption on Ag(111) and Ag_{54}/γ-Al_2O_3 (*vide infra*). Table 1 lists the decomposition results obtained using a conventional DFT method and the dispersion of energy using the D3 method. CO adsorption on Ag is weak, and the contribution of the dispersion interaction is significant. For example, CO adsorption on the Ag(111) surface is mainly due to the dispersion force, and the DFT energy gives repulsive energy. In Figure 3, the energy decomposition of CO adsorption is plotted as a function of the NP height. The contribution of the dispersion slightly decreases as the height decreases, and its contribution to the total energy is between 0.1 and 0.2 eV for all sizes. The contribution of the DFT energy increases as the size decreases. The size dependence of the DFT energy is similar for all shapes above 1.4 nm. However, the size dependence of D_{5h} NPs changes steeply from 1.4 nm. Such sudden changes were not observed in the size dependence of I_h and O_h NPs, indicating that the unique enhancement for D_{5h} NPs with a height smaller than 1.4 nm originates from the electronic structure of the decahedron shape.

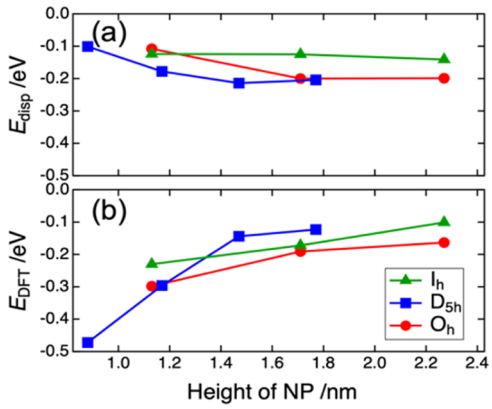

Figure 3. Energy decomposition of CO adsorption energy as a function of the height of NPs. E_{disp} in (a) is the dispersion energy obtained using the D3 method. E_{DFT} in (b) is the contribution of the conventional DFT energy obtained using a conventional DFT method. Adsorption energies on decahedron (D_{5h}), cuboctahedron (O_h), and icosahedron (I_h) are indicated by blue, red, and green marks and lines, respectively.

The perturbation by CO adsorption on the charge density of NPs was examined. Figure 4 shows the charge density

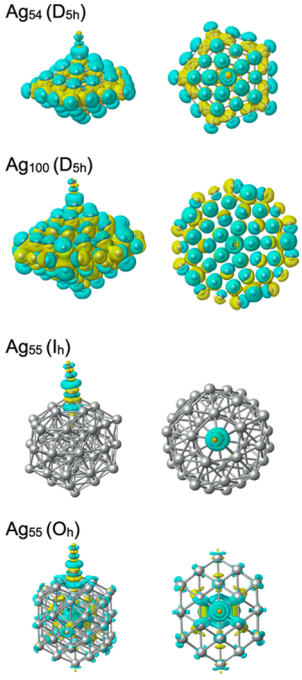

Figure 4. Charge density difference ($\rho_{NP+CO} - \rho_{NP} - \rho_{CO}$) upon CO adsorption. The yellow and cyan scales indicate areas in which electrons are depleted and accumulated, respectively. The plotted contours are chosen to be ($0.001e/Å^3$).

differences by subtracting the charge density of the isolated NPs and CO from that of the adsorbed system. In CO adsorption on the Ag NPs, delocalization in the whole NP is pronounced in the $Ag_{54}(D_{5h})$ NP. This delocalization also occurs in the Ag_{100} (D_{5h}) NP with a height of 1.2 nm, but it is less pronounced than that in the $Ag_{54}(D_{5h})$ NP. For $Ag_{55}(O_h)$ NP and $Ag_{55}(I_h)$ NP, the entire structure is not delocalized, and perturbation occurs locally around the adsorption site. Apart from Au, Ag has no relativistic effect. As a result, the

https://doi.org/10.1021/acsomega.1c06208
ACS Omega 2022, 7, 4405−4412

bonding orbitals between Ag atoms are only s orbitals.[34] There is little mixing of d orbitals with the bonding orbitals. Therefore, the electronic structure of small Ag NPs is often considered using superatom orbitals like Na clusters.[35−37] The superatomic concept shows the electron configuration of $1S^2 1P^6 1D^{10} 2S^2 1F^{14} 2P^6 1G^{15}$ for a spherical Ag_{55} NPs.

Furthermore, point-group symmetry analysis showed the splitting of 1F, 2P, and 1G orbitals in the I_h, O_h, and D_{5h} Ag_{55}^- NPs.[6] The energy levels of the two G orbitals below the Fermi level are located at the same position for the I_h and O_h symmetries. On the other hand, two G orbitals are lowered from the Fermi level for the D_{5h} symmetry. Thus, the superatom states strongly depend on the symmetry of NPs, indicating that the enhancement of CO adsorption on the small D_{5h} NPs is due to the presence of superatom states. Therefore, the difference in the orbital energy levels in these NPs may induce the entire delocalization upon CO adsorption.

NBO analysis was performed to examine how delocalization in D_{5h} NP enhances the binding of CO. The NBO bonding orbitals between CO and Ag NPs are shown in Figure 5. In D_{5h} NPs, the bond is enhanced by the sp hybridization of the Ag orbital, which is weaker in I_h and O_h NPs. Table S2 shows the electronic configuration of Ag at the adsorption site before and after CO adsorption. The electron configuration of a p-orbital increased from 0.3 to 0.9 in D_{5h} NP but from 0.2 to 0.6 in O_h and I_h NPs. As shown in the charge density difference of D_{5h} NP, delocalization occurs throughout the NPs, and charge polarization occurs layer-by-layer. In other words, electronic excitations from s-to p_z-orbitals occur, and delocalization stabilizes such excitations in the D_{5h} NPs. In O_h and I_h NPs, the absence of strong delocalization results in weak hybridization. This is why only the decahedron shows stronger CO adsorption on the apex sites.

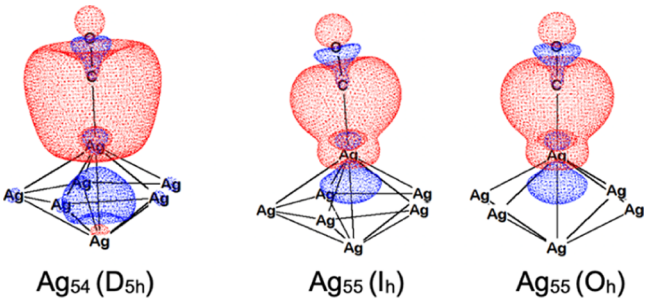

Figure 5. Natural bond orbitals of CO-adsorbed models. Only Ag atoms of the adsorption sites and their neighbors are depicted. The plotted contours are 0.001 e/Å^3.

Structures of Ag NPs/γ-Al_2O_3. Experimental[38−42] and theoretical[38,43] studies have reported that Ag NPs or clusters are positively charged when supported on Al_2O_3. The charged states of NPs may alter the reactivity. Furthermore, the shapes of NPs often change due to the supports. Thus, Ag(D_{5h}) NPs supported on Al_2O_3 may lose the enhancement for CO adsorption by the superatomic states. Therefore, we examined the charged states and shape deformation of the optimized Ag(D_{5h}) NPs on γ-Al_2O_3.

Two types of Ag_{54}-optimized structures on γ-Al_2O_3(110) surfaces were obtained. One is an amorphous structure, and the other contains the local fivefold symmetry on the surface of the Ag NP. AIMD annealing was conducted to reduce the artifact by placing $Ag_{54}(D_{5h})$ on the Al_2O_3 surface by hand. First, the symmetry planes of Ag NP and Al_2O_3 were not aligned but placed so that the (111) plane of the NPs was in contact with Al_2O_3. After AIMD annealing, the structure of the Ag NP was slightly extended to the Al_2O_3 surface while maintaining almost the same structure as in D_{5h} NPs (Figure S2). However, the symmetry was broken entirely upon full geometrical optimization, and an amorphous structure was obtained (Figure 6a,b). This structure is referred to as the Ag_{54}(A) structure.

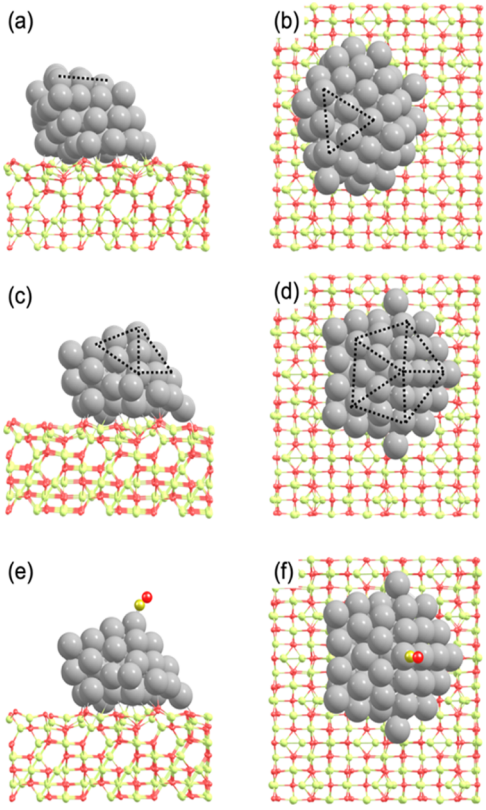

Figure 6. Top and side views of optimized structures of (a,b) Ag_{54}(A)/γ-Al_2O_3, (c,d) Ag_{54}(B)/γ-Al_2O_3, and (e,f) CO-adsorbed Ag_{54}(B)/γ-Al_2O_3. The dark yellow, gray, light yellow, and red balls represent the C, Ag, Al, and O atoms, respectively. The dotted line is a guide to the eye.

When Ag_{54} NPs were placed in the Al_2O_3 hollow, and the symmetry plane of the Ag NP was aligned with that of Al_2O_3, AIMD annealing lifted the Ag NPs from the Al_2O_3 surface, and the Ag NP shape was slightly deformed (Figure S3). The geometrical optimization results in the further deformation of the lower part of Ag NPs and Ag atoms in contact with the Al_2O_3 surface increased. The upper part of the Ag NP holds the local fivefold symmetry. Figure 6c,d shows the optimized structure. This is referred to as the Ag_{54}(B) structure.

The interface atoms of the Ag_{54}(A) and the Ag_{54}(B) structures are shown in Figure 7. The interfacial atoms in the Ag_{54}(A) structure do not have symmetry planes; hence, the structure on these atoms becomes amorphous. In the Ag_{54}(B) structure, the interfacial atoms are symmetrically arranged, reflecting the symmetry of the underlying structure. The average bond length between the Ag atoms at the Ag_{54}(B) interface is 2.90 Å, which is almost the same as 2.93 Å for the isolated $Ag_{54}(D_{5h})$. The absence of drastic changes in the bond

https://doi.org/10.1021/acsomega.1c06208
ACS Omega 2022, 7, 4405−4412

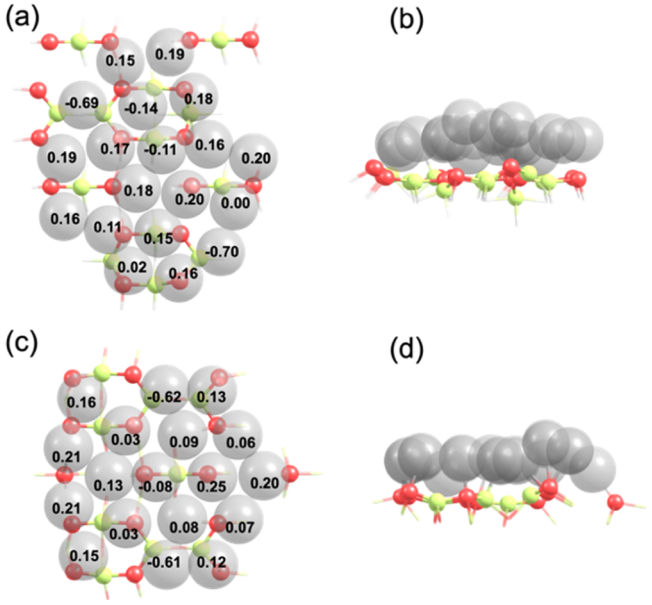

Figure 7. Top and side views of interfacial Ag atoms and Al_2O_3 of $Ag_{54}(A)/\gamma$-Al_2O_3 (a,b) and $Ag_{54}(B)/\gamma$-Al_2O_3 (c,d). Ag, Al, and O atoms are shown as transparent gray, yellow, and red balls, respectively. The numbers in the gray balls are the Bader charges (in e) of Ag atoms.

length results in the fivefold symmetry of the upper part similar to that in the isolated $Ag_{54}(D_{5h})$ NPs.

Bader analysis was performed to examine the charged states of Ag_{54}/γ-Al_2O_3. The Bader charges are summarized in Table S3. Although the structures of $Ag_{54}(A)$ and $Ag_{54}(B)$ on γ-Al_2O_3 are entirely different, the total Ag NP charges are +1|e|. Electron transfer occurs from the NPs to the support. The charge distribution is not uniform in the entire Ag atoms. Bader charges of Ag atoms at the interface are shown in Figure 7a,b. Ag close to oxygen is positively charged and when close to Al is negatively charged, indicating that the Ag atoms interact with both O and Al. The total charge of the interfacial atoms is 0.6|e|, indicating that the interfacial Ag atoms are responsible for 60% of the electron transfer. When the charges of the second layer atoms directly adjacent to the interfacial atoms are added to those of the interfacial atoms, the total charges become almost +1|e|, indicating that the electron transfer is mainly achieved by the two layers of atoms at the interface. The total charges of the top atoms around the adsorption sites are −0.02 and −0.06 for $Ag_{54}(A)/\gamma$-Al_2O_3 and $Ag_{54}(B)/\gamma$-Al_2O_3, respectively. These values are slightly negative, even though the supported Ag NPs show cationic characteristics.

CO Adsorption on Ag NP/γ-Al_2O_3. Geometrical optimization of CO adsorbed on $Ag_{54}(B)/\gamma$-Al_2O_3 was performed. CO was set at the local fivefold symmetric adsorption site, and the optimized structures are shown in Figure 6e,f. The top view of the supported $Ag_{54}(B)$ appears to have a fivefold symmetry similar to that of the isolated $Ag_{54}(D_{5h})$ NPs. However, the adsorption style of CO is different. CO in the optimized structure is tilted in the adsorption site. The adsorption energy is −0.48 eV, which is lower than that of the isolated $Ag_{54}(D_{5h})$ (−0.57 eV) but higher than that of the isolated $Ag_{55}(I_h)$ and $Ag_{55}(O_h)$. The local environment around the adsorption site on $Ag_{54}(B)/\gamma$-Al_2O_3 could not reproduce the adsorption site on the isolated $Ag_{54}(D_{5h})$. Figure 8 shows the perturbation of

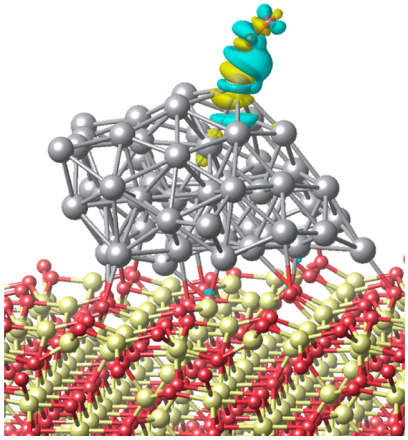

Figure 8. Charge density difference upon CO adsorption on $Ag_{54}(B)/\gamma$-Al_2O_3. The yellow and cyan scales indicate areas in which electrons are depleted and accumulated, respectively, and the dark yellow, gray, yellow, and red balls represent C, Ag, Al, and O atoms, respectively.

charge density by CO adsorption. Perturbation occurred in the local region around the adsorption site, but no perturbation was observed in the bottom part of the Ag NPs and the support. The loss of the high symmetry of the Ag NP structure resulted in the disappearance of the strong delocalization, which indicates the enhancement of CO adsorption.

Because there was no enhancement due to superatomic states, a moderate size effect is expected in CO adsorption on $Ag_{54}(B)/\gamma$-Al_2O_3. Although the overall $Ag_{54}(B)$ charge is +1 due to the charge transfer to the support, the local charge around the adsorption site is comparable to that of the neutral D_{5h} NPs (Table S3). Because the adsorbed CO is almost neutral, charge polarization at the interface between the support and Ag NPs slightly affects the adsorption. Although only two points showed a moderate size dependence of the isolated D_{5h} NPs, the slope (0.10) is the same as that of the isolated I_h NPs. Thus, the linear size effect for D_{5h} NPs can be applied to Ag54(B), whose structure is deformed from the perfect D_{5h} symmetry. Using the linearity dependence of the size on the adsorption energy for D_{5h} NPs, the CO adsorption energy for $Ag_{54}(B)$ with a height of about 0.84 nm was calculated to be −0.43 eV, which is comparable to the CO adsorption energy for $Ag_{54}(B)/\gamma$-Al_2O_3 (−0.48 eV). Thus, it indicates that the moderate size effect is valid for the adsorption of neutral adsorbates on Ag NPs with a low symmetry supported by γ-Al_2O_3. In contrast to the isolated Ag NPs, the loss of the high symmetry of the supported Ag NPs leads to the disappearance of the boosted size effect observed in the isolated D_{5h} NPs.

CONCLUSIONS

We conducted a DFT study on Ag NPs supported on γ-Al_2O_3. First, we studied the isolated Ag NPs with various sizes for CO adsorption: decahedral (D_{5h}), icosahedral (I_h), and cuboctahedral (O_h) structures. To evaluate the size effect, care must be taken in the choice of the size direction as a descriptor because it affects the potential that determines the electronic state of the adsorption site. Therefore, we used the height of the NPs as a descriptor of CO adsorption on the apex sites of Ag NPs. An increased size effect was observed only for D_{5h} NPs with a height below 1.4 nm, which is attributed to the interaction between CO and superatomic states, leading to the electron

https://doi.org/10.1021/acsomega.1c06208
ACS Omega 2022, 7, 4405−4412

density delocalization into the entire NP structure by CO adsorption. Such delocalization did not occur in the I_h and O_h NPs, which shows a moderate size effect.

Next, we performed the geometrical optimization of the Ag_{54} decahedral structure on the γ-$Al_2O_3(110)$ surface in combination with an AIMD procedure. Two types of structures were obtained: an amorphous structure [Ag_{54}(A)] and a locally fivefold symmetrical structure [Ag_{54}(B)]. In the latter structure, the Ag atoms at the interface maintain the symmetry reflected in the substrate surface. CO adsorption on Ag_{54}(B) is weaker than that on the isolated D_{5h} Ag NP due to the loss of high symmetry. Although both Ag_{54}(A) and Ag_{54}(B) are positively charged, electron transfer to the support occurs only from the Ag atoms in the lower two layers of the NPs. We observed that Ag NPs with two layers in height have highly charged surface Ag atoms supported by Al_2O_3. Because the Ag atoms on the top of Ag NPs with three or more layers in height become neutral, the drastic size effect in height would be observed in adsorption involving charge transfer, such as oxygen adsorption.

COMPUTATIONAL METHODS

All the spin-polarized density functional theory (DFT) calculations were performed using the Vienna Ab initio Simulation Package (VASP).[16−18] The generalized gradient approximation in RPBE[19] was used as the correlation and exchange energy functional. The RPBE functional is suitable for calculating adsorption energies but not for describing bulk properties (Table S4). However, with the addition of the dispersion force correction by the Grimme's D3 method,[20] the bulk lattice parameter and cohesive energy are close to the experimental values. Furthermore, the CO adsorption energy on an Ag(111) surface is in good agreement with the experiment. The electron−ion interaction with the frozen-core approximation was described using the projector augmented wave (PAW) method.[21] Wavefunctions for valence electrons were represented using a periodic-wave basis set with a cutoff energy of 430 eV. We also used the Methfessel−Paxton broadening method[22] with a smearing width of 0.1 eV to improve the convergence of states near the Fermi level. Structural optimization was performed until the energy and force converged within criteria of 1.0×10^{-5} eV and 0.01 eV/Å, respectively. The vacuum spacing for the isolated molecule and Ag NPs was set to a 12 Å. A 3×3 supercell model (25.02 × 24.08 Å) of dehydrated γ-$Al_2O_3(110)$[23] consists of eight atomic layers. This slab model has 630 atoms. The vacuum spacing of the slab model was set to 24 Å along the z-direction because the Ag_{54} NP with a height of 8.8 Å was located on this surface. In the geometry optimization of Ag_{54} on the $Al_2O_3(110)$, an ab-initio molecular dynamics (AIMD) annealing procedure described below was employed to reduce the artifacts by placing Ag_{54} on the Al_2O_3 by hand. First, annealing was conducted for 400 fs at 25 K using NVT AIMD, followed by 800 fs holding at 100 K. We used a Nosé−Hoover thermostat[24,25] with a time step of 4 fs. This AIMD procedure was enough to diffuse Ag atoms from the unstable site of the Al_2O_3 surface to the stable adsorption sites. Geometry optimization of Ag_{54}/Al_2O_3 was performed, starting from the initial structure obtained through the AIMD procedure. The top four atomic layers of this slab were allowed to relax, and the rest of the bottom atoms were fixed. For the sampling of the reciprocal space, only the gamma point was sampled because the nonperiodic NPs and size of the Al_2O_3 slab model were enough to produce reliable energy. For Bader charge analysis, the program developed by the Henkelman group was used.[26] Charge density differences were plotted using VESTA.[27] Adsorption energies E_{ads} were calculated according to the following equation

$$E_{ads} = E_{tot} - E_M - E_{CO}$$

where E_{tot} is the total energy of CO adsorbed on Ag NP, E_M is the energy of the uncovered Ag NP, and E_{CO} is the energy of CO in the gas phase. Thus, the negative value means stable adsorption. Natural bond orbitals (NBOs) were calculated at the PBEPBE/def2-SVP level using Gaussian 16.[28]

ASSOCIATED CONTENT

Supporting Information

The Supporting Information is available free of charge at https://pubs.acs.org/doi/10.1021/acsomega.1c06208.

Size of Ag nanoparticles, natural electron configuration of adsorption sites, Bader charges before and after CO adsorption, comparison between experimental and calculated values of Ag bulk property, illustration of the definition of width and height, initial geometry, and coordinates of optimized structures (PDF)

AUTHOR INFORMATION

Corresponding Author

Kyoichi Sawabe − *Department of Materials Chemistry, Graduate School of Engineering, Nagoya University, Nagoya 464-8603, Japan; Elements Strategy Initiative for Catalysts and Batteries, Kyoto University, Kyoto 615-8245, Japan;* orcid.org/0000-0001-6228-1395; Email: sawabe@chembio.nagoya-u.ac.jp

Author

Atsushi Satsuma − *Department of Materials Chemistry, Graduate School of Engineering, Nagoya University, Nagoya 464-8603, Japan; Elements Strategy Initiative for Catalysts and Batteries, Kyoto University, Kyoto 615-8245, Japan;* orcid.org/0000-0001-6946-7678

Complete contact information is available at: https://pubs.acs.org/10.1021/acsomega.1c06208

Notes

The authors declare no competing financial interest.

ACKNOWLEDGMENTS

This study was performed under the management of the Elements Strategy Initiative for Catalysts & Batteries (ESICB, JPMXP0112101003), which is supported by the Ministry of Education, Culture, Sports, Science, and Technology. We used the supercomputer of ACCMS, Kyoto University.

ABBREVIATIONS

AIMD, ab initio molecular dynamics; CN, coordination number; DFT, density functional theory; NBO, natural bond orbitals; PAW, projector augmented wave; VASP, Vienna ab initio simulation package

REFERENCES

(1) Cuenya, B. R. Synthesis and Catalytic Properties of Metal Nanoparticles: Size, Shape, Support, Composition, and Oxidation State Effects. *Thin Solid Films* **2010**, *518*, 3127−3150.

(2) Van Hardeveld, R.; Hartog, F. The Statistics of Surface Atoms and Surface Sites on Metal Crystals. *Surf. Sci.* **1969**, *15*, 189−230.
(3) Kleis, J.; Greeley, J.; Romero, N. A.; Morozov, V. A.; Falsig, H.; Larsen, A. H.; Lu, J.; Mortensen, J. J.; Dułak, M.; Thygesen, K. S.; Nørskov, J. K.; Jacobsen, K. W. Finite Size Effects in Chemical Bonding: From Small Clusters to Solids. *Catal. Lett.* **2011**, *141*, 1067−1071.
(4) Li, L.; Larsen, A. H.; Romero, N. A.; Morozov, V. A.; Glinsvad, C.; Abild-Pedersen, F.; Greeley, J.; Jacobsen, K. W.; Nørskov, J. K. Investigation of Catalytic Finite-Size-Effects of Platinum Metal Clusters. *J. Phys. Chem. Lett.* **2013**, *4*, 222−226.
(5) Mingos, D. M. P. Structural and Bonding Patterns in Gold Clusters. *Dalton Trans.* **2015**, *44*, 6680−6695.
(6) Kaappa, S.; Malola, S.; Häkkinen, H. Point Group Symmetry Analysis of the Electronic Structure of Bare and Protected Metal Nanocrystals. *J. Phys. Chem. A* **2018**, *122*, 8576−8584.
(7) Takei, T.; Akita, T.; Nakamura, I.; Fujitani, T.; Okumura, M.; Okazaki, K.; Huang, J.; Ishida, T.; Haruta, M. Heterogeneous Catalysis by Gold. *Advances in Catalysis*; Elsevier, 2012; Vol. *55*, pp 1−126.
(8) Cunningham, D. A. H.; Vogel, W.; Sanchez, R. M. T.; Tanaka, K.; Haruta, M. Structural Analysis of Au/TiO_2 Catalysts by Debye Function Analysis. *J. Catal.* **1999**, *183*, 24−31.
(9) Ishida, T.; Murayama, T.; Taketoshi, A.; Haruta, M. Importance of Size and Contact Structure of Gold Nanoparticles for the Genesis of Unique Catalytic Processes. *Chem. Rev.* **2020**, *120*, 464−525.
(10) Lopez, N. On the Origin of the Catalytic Activity of Gold Nanoparticles for Low-Temperature CO Oxidation. *J. Catal.* **2004**, *223*, 232−235.
(11) Murata, K.; Mahara, Y.; Ohyama, J.; Yamamoto, Y.; Arai, S.; Satsuma, A. The Metal-Support Interaction Concerning the Particle Size Effect of Pd/Al_2O_3 on Methane Combustion. *Angew. Chem.* **2017**, *129*, 16209−16213.
(12) Shimizu, K.-i.; Sawabe, K.; Satsuma, A. Self-Regenerative Silver Nanocluster Catalyst for CO Oxidation. *ChemCatChem* **2011**, *3*, 1290−1293.
(13) Dutov, V. V.; Mamontov, G. V.; Zaikovskii, V. I.; Vodyankina, O. V. The effect of support pretreatment on activity of Ag/SiO_2 catalysts in low-temperature CO oxidation. *Catal. Today* **2016**, *278*, 150−156.
(14) Wang, F.; Li, Z.; Wang, H.; Chen, M.; Zhang, C.; Ning, P.; He, H. Nano-Sized Ag Rather than Single-Atom Ag Determines CO Oxidation Activity and Stability. *Nano Res* **2022**, *15*, 452.
(15) Tamaru, K. Characteristic Behavior of Chemisorbed Oxygen on Silver in the Reaction with Carbon Monoxide. *J. Mol. Catal. A: Chem.* **2000**, *163*, 3−7.
(16) Kresse, G.; Hafner, J. Ab initiomolecular dynamics for liquid metals. *Phys. Rev. B: Condens. Matter Mater. Phys.* **1993**, *47*, 558−561.
(17) Kresse, G.; Furthmüller, J. Efficient iterative schemes forab initiototal-energy calculations using a plane-wave basis set. *Phys. Rev. B: Condens. Matter Mater. Phys.* **1996**, *54*, 11169−11186.
(18) Kresse, G.; Furthmüller, J. Efficiency of Ab-Initio Total Energy Calculations for Metals and Semiconductors Using a Plane-Wave Basis Set. *Comput. Mater. Sci.* **1996**, *6*, 15−50.
(19) Hammer, B.; Hansen, L. B.; Nørskov, J. K. Improved Adsorption Energetics within Density-Functional Theory Using Revised Perdew-Burke-Ernzerhof Functionals. *Phys. Rev. B: Condens. Matter Mater. Phys.* **1999**, *59*, 7413−7421.
(20) Grimme, S.; Antony, J.; Ehrlich, S.; Krieg, H. A Consistent and Accurate Ab Initio Parametrization of Density Functional Dispersion Correction (DFT-D) for the 94 Elements H-Pu. *J. Chem. Phys.* **2010**, *132*, 154104.
(21) Blöchl, P. E. Projector Augmented-Wave Method. *Phys. Rev. B: Condens. Matter Mater. Phys.* **1994**, *50*, 17953−17979.
(22) Methfessel, M.; Paxton, A. T. High-Precision Sampling for Brillouin-Zone Integration in Metals. *Phys. Rev. B: Condens. Matter Mater. Phys.* **1989**, *40*, 3616−3621.
(23) Digne, M.; Sautet, P.; Raybaud, P.; Euzen, P.; Toulhoat, H. Use of DFT to achieve a rational understanding of acid?basic properties of ?-alumina surfaces. *J. Catal.* **2004**, *226*, 54−68.
(24) Nosé, S. A Unified Formulation of the Constant Temperature Molecular Dynamics Methods. *J. Chem. Phys.* **1984**, *81*, 511−519.
(25) Hoover, W. G. Canonical Dynamics: Equilibrium Phase-Space Distributions. *Phys. Rev. A: At., Mol., Opt. Phys.* **1985**, *31*, 1695−1697.
(26) Henkelman, G.; Arnaldsson, A.; Jónsson, H. A Fast and Robust Algorithm for Bader Decomposition of Charge Density. *Comput. Mater. Sci.* **2006**, *36*, 354−360.
(27) Momma, K.; Izumi, F. VESTA 3for three-dimensional visualization of crystal, volumetric and morphology data. *J. Appl. Crystallogr.* **2011**, *44*, 1272−1276.
(28) Frisch, M. J.; Trucks, G. W.; Schlegel, H. B.; Scuseria, G. E.; Robb, M. A.; Cheeseman, J. R.; Scalmani, G.; Barone, V.; Petersson, G. A.; Nakatsuji, H.; Li, X.; Caricato, M.; Marenich, A. V.; Bloino, J.; Janesko, B. G.; Gomperts, R.; Mennucci, B.; Hratchian, H. P.; Ortiz, J. V.; Izmaylov, A. F.; Sonnenberg, J. L.; Williams-Young, D.; Ding, F.; Lipparini, F.; Egidi, F.; Goings, J.; Peng, B.; Petrone, A.; Henderson, T.; Ranasinghe, D.; Zakrzewski, V. G.; Gao, J.; Rega, N.; Zheng, G.; Liang, W.; Hada, M.; Ehara, M.; Toyota, K.; Fukuda, R.; Hasegawa, J.; Ishida, M.; Nakajima, T.; Honda, Y.; Kitao, O.; Nakai, H.; Vreven, T.; Throssell, K.; Montgomery, J. A., Jr; Peralta, J. E.; Ogliaro, F.; Bearpark, M. J.; Heyd, J. J.; Brothers, E. N.; Kudin, K. N.; Staroverov, V. N.; Keith, T. A.; Kobayashi, R.; Normand, J.; Raghavachari, K.; Rendell, A. P.; Burant, J. C.; Iyengar, S. S.; Tomasi, J.; Cossi, M.; Millam, J. M.; Klene, M.; Adamo, C.; Cammi, R.; Ochterski, J. W.; Martin, R. L.; Morokuma, K.; Farkas, O.; Foresman, J. B.; Fox, D. J. *Gaussian 16* Revision C.01; Gaussian, Inc.: Wallingford CT, 2016.
(29) Laletina, S. S.; Mamatkulov, M.; Shor, E. A.; Kaichev, V. V.; Genest, A.; Yudanov, I. V.; Rösch, N. Size-Dependence of the Adsorption Energy of CO on Pt Nanoparticles: Tracing Two Intersecting Trends by DFT Calculations. *J. Phys. Chem. C* **2017**, *121*, 17371−17377.
(30) Yudanov, I. V.; Genest, A.; Schauermann, S.; Freund, H.-J.; Rösch, N. Size Dependence of the Adsorption Energy of CO on Metal Nanoparticles: A DFT Search for the Minimum Value. *Nano Lett.* **2012**, *12*, 2134−2139.
(31) Sawabe, K.; Koketsu, T.; Ohyama, J.; Satsuma, A. A Theoretical Insight into Enhanced Catalytic Activity of Au by Multiple Twin Nanoparticles. *Catalysts* **2017**, *7*, 191.
(32) Johnson, C. L.; Snoeck, E.; Ezcurdia, M.; Rodríguez-González, B.; Pastoriza-Santos, I.; Liz-Marzán, L. M.; Hÿtch, M. J. Effects of Elastic Anisotropy on Strain Distributions in Decahedral Gold Nanoparticles. *Nat. Mater.* **2008**, *7*, 120−124.
(33) Ino, S. Stability of Multiply-Twinned Particles. *J. Phys. Soc. Jpn.* **1969**, *27*, 941−953.
(34) Lee, H. M.; Ge, M.; Sahu, B. R.; Tarakeshwar, P.; Kim, K. S. Geometrical and Electronic Structures of Gold, Silver, and Gold−Silver Binary Clusters: Origins of Ductility of Gold and Gold−Silver Alloy Formation. *J. Phys. Chem. B* **2003**, *107*, 9994−10005.
(35) de Heer, W. A. The Physics of Simple Metal Clusters: Experimental Aspects and Simple Models. *Rev. Mod. Phys.* **1993**, *65*, 611−676.
(36) Omoda, T.; Takano, S.; Tsukuda, T. Toward Controlling the Electronic Structures of Chemically Modified Superatoms of Gold and Silver. *Small* **2021**, *17*, 2001439.
(37) He, X.; Walter, M.; Jiang, D. E. Understanding Superatomic Ag Nanohydrides. *Small* **2021**, *17*, 2004808.
(38) Deng, H.; Yu, Y.; Liu, F.; Ma, J.; Zhang, Y.; He, H. Nature of Ag Species on Ag/γ-Al2O3: A Combined Experimental and Theoretical Study. *ACS Catal.* **2014**, *4*, 2776−2784.
(39) Korhonen, S. T.; Beale, A. M.; Newton, M. A.; Weckhuysen, B. M. New Insights into the Active Surface Species of Silver Alumina Catalysts in the Selective Catalytic Reduction of NO. *J. Phys. Chem. C* **2011**, *115*, 885−896.
(40) Shimizu, K.-i.; Tsuzuki, M.; Kato, K.; Yokota, S.; Okumura, K.; Satsuma, A. Reductive Activation of O_2 with H_2-Reduced Silver Clusters as a Key Step in the H_2-Promoted Selective Catalytic

https://doi.org/10.1021/acsomega.1c06208
ACS Omega 2022, 7, 4405−4412

Reduction of NO with C_3H_8 over Ag/Al_2O_3. *J. Phys. Chem. C* **2007**, *111*, 950−959.
(41) Breen, J. P.; Burch, R.; Hardacre, C.; Hill, C. J. Structural Investigation of the Promotional Effect of Hydrogen during the Selective Catalytic Reduction of NOx with Hydrocarbons over Ag/Al_2O_3 Catalysts. *J. Phys. Chem. B* **2005**, *109*, 4805−4807.
(42) She, X.; Flytzanistephanopoulos, M. The role of Ag-O-Al species in silver-alumina catalysts for the selective catalytic reduction of NO_x with methane. *J. Catal.* **2006**, *237*, 79−93.
(43) Hirunsit, P.; Shimizu, K.-i.; Fukuda, R.; Namuangruk, S.; Morikawa, Y.; Ehara, M. Cooperative H2 Activation at Ag Cluster/θ-Al_2O_3(110) Dual Perimeter Sites: A Density Functional Theory Study. *J. Phys. Chem. C* **2014**, *118*, 7996−8006.

https://doi.org/10.1021/acsomega.1c06208
ACS Omega 2022, 7, 4405−4412